



HAL
open science

Oxidation of 316L(N) Stainless Steel in Liquid Sodium at 650 °C

Matthieu Rivollier, J. L. Courouau, Michel Tabarant, Cécile Blanc,
Marie-Laurence Giorgi

► **To cite this version:**

Matthieu Rivollier, J. L. Courouau, Michel Tabarant, Cécile Blanc, Marie-Laurence Giorgi. Oxidation of 316L(N) Stainless Steel in Liquid Sodium at 650 °C. *Journal of Nuclear Materials*, 2018, 500, pp.337 - 348. 10.1016/j.jnucmat.2017.12.037 . hal-01810057

HAL Id: hal-01810057

<https://centralesupelec.hal.science/hal-01810057>

Submitted on 7 Jun 2018

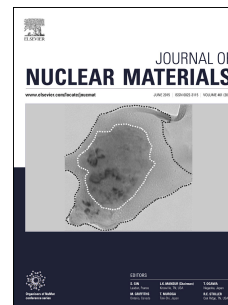
HAL is a multi-disciplinary open access archive for the deposit and dissemination of scientific research documents, whether they are published or not. The documents may come from teaching and research institutions in France or abroad, or from public or private research centers.

L'archive ouverte pluridisciplinaire **HAL**, est destinée au dépôt et à la diffusion de documents scientifiques de niveau recherche, publiés ou non, émanant des établissements d'enseignement et de recherche français ou étrangers, des laboratoires publics ou privés.

Accepted Manuscript

Oxidation of 316L(N) stainless steel in liquid sodium at 650□°C

Matthieu Rivollier, Jean-Louis Courouau, Michel Tabarant, Cécile Blanc, Marie-Laurence Giorgi



PII: S0022-3115(17)31275-8

DOI: [10.1016/j.jnucmat.2017.12.037](https://doi.org/10.1016/j.jnucmat.2017.12.037)

Reference: NUMA 50702

To appear in: *Journal of Nuclear Materials*

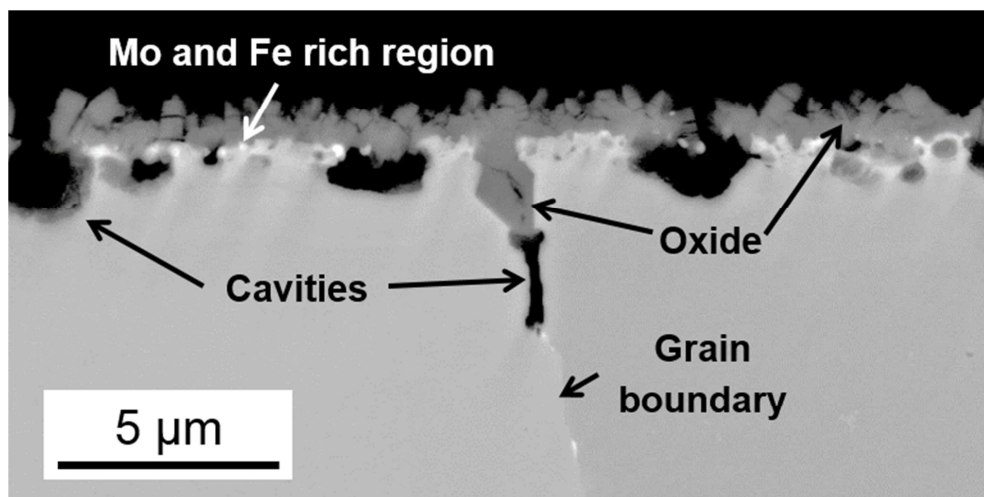
Received Date: 19 September 2017

Revised Date: 5 December 2017

Accepted Date: 24 December 2017

Please cite this article as: M. Rivollier, J.-L. Courouau, M. Tabarant, Cé. Blanc, M.-L. Giorgi, Oxidation of 316L(N) stainless steel in liquid sodium at 650□°C, *Journal of Nuclear Materials* (2018), doi: 10.1016/j.jnucmat.2017.12.037.

This is a PDF file of an unedited manuscript that has been accepted for publication. As a service to our customers we are providing this early version of the manuscript. The manuscript will undergo copyediting, typesetting, and review of the resulting proof before it is published in its final form. Please note that during the production process errors may be discovered which could affect the content, and all legal disclaimers that apply to the journal pertain.



15 **Abstract**

16 The corrosion of an austenitic steel in liquid sodium containing $189 \mu\text{g.g}^{-1}$ of oxygen was
17 investigated at 650°C as a function of time (122, 250 and 500 h). The steel samples were
18 characterized by means of complementary techniques, namely scanning electron microscopy, X-
19 ray diffraction, glow discharge optical emission spectroscopy and transmission electron
20 microscopy. The characterizations showed that a NaCrO_2 oxide scale forms at the steel surface.
21 Under this oxide scale, iron and molybdenum rich M_6C carbide particles together with NaCrO_2 in
22 the grain boundaries and cavities filled with sodium were observed. The stainless steel substrate
23 and / or the chromite scale were dissolved in parallel with the formation of chromite and carbides.
24 Thermodynamic calculations showed that NaCrO_2 and M_6C are equilibrium phases in such a
25 system. NaCrO_2 is formed by the reaction of chromium diffusing from the steel bulk with sodium
26 and dissolved oxygen (external selective oxidation). Mo segregates to the steel surface where it
27 reacts with Fe from the steel and C dissolved in liquid sodium. The dissolution of stainless steel
28 occurred since the liquid sodium bath is not saturated in the dissolving species (pure metals and
29 oxides such as NaCrO_2 , Na_4FeO_3). As for the cavities, vacancies are created at the steel / NaCrO_2
30 interface by Cr oxidation, carburization and dissolution of the other elements present in the
31 stainless steel. The vacancies become supersaturated and this leads to the nucleation of the
32 cavities observed. Part of the vacancies created by Cr oxidation or steel dissolution is annihilated
33 at sinks like dislocations leading to the translation of the oxide / metal interface towards the metal
34 bulk.

35 **Keywords: liquid sodium, austenitic steel, high temperature corrosion, selective oxidation**

36

37 **1. Introduction**

38 France made plans to construct the fourth generation of nuclear reactor and chose the Sodium-
39 Cooled Fast Reactor (SFR) as the technology to develop. The expected economically reasonable
40 service life-time of a reactor is 60 years. In these reactors, liquid sodium Na is used as a coolant
41 at high temperatures (400 to 550°C for the liquid metal bulk and up to 650°C at the hot spots of
42 the fuel claddings) [1]. As the chemical conditions can change with time (normal, transient and
43 incidental), any interactions between the liquid metal and the structural materials (made mainly
44 of austenitic steels) must be well known, well understood and predicted to guarantee service life-
45 time as well as resistance to incidental conditions.

46 In sodium-cooled fast reactors, the liquid metal oxygen content is maintained at a maximum of
47 $10 \mu\text{g}\cdot\text{g}^{-1}$ by means of purification systems, in order to prevent solid oxide from precipitating in
48 the circulation loops and minimize corrosion of the structural materials. However, certain events
49 such as air or water leaks could occur during the service life-time of the nuclear reactor, leading
50 to a temporary increase in the dissolved oxygen content ($15 \mu\text{g}\cdot\text{g}^{-1}$ to $200 \mu\text{g}\cdot\text{g}^{-1}$ for unexpected
51 transient) [2].

52 For austenitic steels immersed in liquid sodium containing low oxygen levels (less than $10 \mu\text{g}\cdot\text{g}^{-1}$
53 ¹⁾ for a few hundred or thousand hours, the corrosion is mainly due to the preferential dissolution
54 of nickel and, to a lesser extent, chromium and manganese. This preferential dissolution leads to
55 the ferritization of the steel surface. The thickness of the ferrite layer formed is of the order of a
56 few μm [3-8]. At longer immersion times, austenitic steels are dissolved homogeneously with a
57 kinetic attributed to iron dissolution [3,4]. An increase in the oxygen content or in the
58 temperature is reported to increase the dissolution rate [4,6,7,9]. This is explained by an increase

59 of the iron solubility in sodium in presence of oxygen [10, 11]. Kolster et al. [12] show that
60 oxygen might also increase the preferential dissolution rate of chromium, due to the formation of
61 a Na-Cr-O dissolved complex.

62 At higher oxygen contents in liquid sodium, i.e. more than $15 \mu\text{g}\cdot\text{g}^{-1}$ [8,13], oxide scales rich in
63 Na and Cr are formed on the surface of austenitic or ferritic / martensitic steels. This oxide is
64 $\text{Na}_2\text{O}\cdot\text{Cr}_2\text{O}_3$, also called sodium chromite NaCrO_2 [8,9,14-16]. An increase in the oxygen content
65 or in the temperature is reported to increase the oxidation rate [13-15]. The NaCrO_2 formation
66 causes Cr depletion in the steel under the oxide scale, for both ferritic / martensitic [15,17] and
67 austenitic steels [15]. In this case, the steel grain boundaries can be enriched in Na and O [14].

68 A discontinuous phase rich in Mo can also be formed at the surface or subsurface of steels
69 containing Mo immersed in liquid sodium [3]. This phase could be Fe_7Mo_6 or M_6C type carbides
70 at temperatures higher than 650°C , M being Cr, Mn, Fe, Ni or Mo (liquid sodium contains traces
71 of C) [8]. For instance, $\text{Fe}_4\text{Mo}_2\text{C}$ was detected as shown in ref. [9].

72 Finally, it can be concluded from this literature review that the mechanisms involved in the
73 corrosion of austenitic steels in liquid sodium are very complex and not yet fully understood [18].
74 In recent years, as the experiments using liquid Na are not easy to perform, there are few studies
75 on the corrosion in liquid Na. The influence of immersion time and dissolved oxygen content is
76 not studied precisely enough to be confident in the results that could be obtained at long
77 immersion times. The primary goal of our study, therefore, is to gain a better understanding of the
78 corrosion mechanisms involved in liquid sodium in controlled temperature and oxygen content
79 conditions and to investigate further a key step in the corrosion process: Cr diffusion from the
80 steel bulk to the steel surface. The work is divided into the following stages:

- 81 1) Immersion of the chosen austenitic steel in liquid Na containing $189 \mu\text{g.g}^{-1}$ of oxygen at 650°C
82 for different immersion times up to 500 h;
- 83 2) Characterization of the samples obtained to determine the nature and composition of the
84 corrosion products and estimate the oxidation depth;
- 85 3) Measurement of chromium concentration profiles in the vicinity of grain boundaries;
- 86 4) Discussion on the key mechanisms explaining the corrosion of austenitic steels in liquid sodium.

87

88 **2. Materials and corrosion conditions**

89 **2.1. Stainless steel and sodium**

90 The substrate tested is an austenitic stainless steel 316L(N) (provided by Industeel France). The
91 dimensions of the steel specimens were 30 mm long, 20 mm wide and 1.5 mm thick. A 1 mm
92 diameter hole along thickness took place at 3 mm from edge in the middle of the width. Its
93 composition is given in Table 1. The analysis was performed using induced coupled plasma
94 atomic spectroscopy and glow discharge optical emission spectroscopy for carbon. The grain size
95 is close to $41 \pm 2 \mu\text{m}$ (Fig. 1). Before the corrosion experiments, the specimens were polished in
96 several stages. In order to study the influence of the steel surface roughness on corrosion in liquid
97 sodium, it was decided to stop the mechanical polishing at different stages (1200 and 4000 grit
98 SiC paper and $1 \mu\text{m}$ diamond suspension). The surface roughness obtained with this procedure
99 was found to have a negligible influence on corrosion in liquid sodium during our trials (average
100 roughness $Ra < 0.1 \mu\text{m}$). Therefore, the sample surface roughness is not given for the results
101 described below.

102 High purity sodium (99.95 wt.%) was provided by Métaux Spéciaux SA. The principal impurities
103 are $[Ca] < 2 \mu\text{g}\cdot\text{g}^{-1}$, $[Cl] = 4 \mu\text{g}\cdot\text{g}^{-1}$, $[Fe] = 1 \mu\text{g}\cdot\text{g}^{-1}$, $[K] = 4 \mu\text{g}\cdot\text{g}^{-1}$. It also contains traces of C.
104 The quantitative analysis of carbon was not possible in our conditions due to contamination
105 during analysis procedure. However, the experimental conditions of the test were already
106 observed as carburizing for this low carbon steel [18]. The as-received solid sodium is covered
107 with a sodium oxide layer, which is manually removed inside an argon-atmosphere glovebox.

108

109 **2.2. Experimental conditions**

110 The corrosion tests were run in a static sodium device called CorroNa [2]. The sodium (2.3 kg) is
111 contained in a molybdenum crucible (MLR grade containing 0.7 wt.% of La_2O_3 , Plansee), placed
112 in a resistance heated furnace. Molybdenum dissolution in sodium was reported to be negligible
113 in molybdenum-made circuit [12]. The device is set in a purified argon atmosphere (provided by
114 Messer with a purity index 6.0, i.e. less than 3 vpm of H_2O and 2 vpm of oxygen and purified by
115 zeolite adsorption), inside a glove box to simplify all operations involving preparing the test and
116 handling the liquid metal. During the corrosion tests, the system containing the liquid sodium in
117 contact with pure argon is perfectly sealed off from the argon atmosphere in the glove box.

118 After sodium melting, solid sodium oxides float to the free surface of the liquid metal, probably
119 due to surface tension effects, allowing a first skimming operation to be performed to remove
120 these sodium oxides. The liquid metal is then held at low temperature ($105\text{-}110^\circ\text{C}$) for 3 days.

121 The new floating oxide is then carefully skimmed off from the free surface. An additional
122 purification step is then performed at a high temperature (650°C for 72 h), using a zirconium
123 getter immersed in the liquid bath to eliminate any residual oxide and dissolved oxygen. The

124 estimated dissolved oxygen content obtained after this purification step is $1 \mu\text{g}\cdot\text{g}^{-1}$ at the most.
125 The dissolved zirconium concentration is known to be very low. For instance, at 722°C , the
126 zirconium solubility in sodium is $0.09 \mu\text{g}\cdot\text{g}^{-1}$ [19].
127 After purification, the liquid sodium bath is cooled to 120°C and the zirconium getter is removed.
128 Sodium oxide powder ($\text{Na}_2\text{O} + 14.1 \text{ wt.}\% \text{ Na}_2\text{O}_2$, provided by Alfa Aesar) is added to the liquid
129 sodium in order to obtain an oxygen concentration of $189 \pm 8 \mu\text{g}\cdot\text{g}^{-1}$ (assuming that the initial
130 oxygen concentration in the liquid sodium is equal to zero and that Na_2O and Na_2O_2 are
131 completely dissolved in the liquid Na).
132 After this step, in order to keep the oxygen content of the sodium constant, the specimens are
133 immersed in the molten sodium bath at 120°C and the system is tightly closed. The sodium is
134 then heated to 650°C at a rate of $0.5^\circ\text{C}/\text{min}$. The temperature is kept constant for 122 h, 250 h
135 and 500 h before being decreased at a rate of $0.5^\circ\text{C}/\text{min}$. The specimens are removed from the
136 liquid sodium at 120°C . The sodium residues present on the specimens are removed with 99.9
137 wt.% pure ethanol (provided by Carlo Erba) at ambient temperature. This soft cleaning procedure
138 was chosen to remove the sodium residues from the surface and to keep as much as possible
139 liquid sodium that might have penetrated into the corrosion surface layer during the corrosion
140 processes.

141

142 **2.3. Characterization techniques**

143 Specimens are weighted before and after the corrosion test, using an AT20 weighing scale
144 constructed by MettlerToledo. X-Ray Diffraction (XRD, Bruker D8 discover) was carried out to
145 characterize the phases formed during corrosion. XRD was performed in the θ - 2θ configuration

146 with a copper cathode emitting X-rays of wavelength $\lambda = 1.5406 \text{ \AA}$. Characterizations were
147 performed by means of Scanning Electron Microscopy (SEM, Zeiss LEO 1460VP) associated
148 with Energy Dispersive X-ray spectroscopy (EDX, SAMX DXP-X10P), to observe and analyse
149 the surfaces and polished cross-sections of the specimens. Elementary depth profiles were
150 obtained from the sample surface using Glow Discharge Optical Emission Spectroscopy
151 (GDOES). The instrument used was a GD-Profilier 2 from the Horiba Scientific company. The
152 glow discharge was powered by a 13.56 MHz radio-frequency generator. A 4 mm-diameter
153 copper anode and 99.9999 vol.% purity argon gas were used to sputter the sample (800 Pa and 30
154 W). The emission responses from the excited sputtered elements (O, Fe, Cr, Ni, Mo, C, Si, Mn,
155 etc.) were detected using a polychromator with a focal length of 500 mm. A monochromator was
156 used to determine the sodium concentration. The calibration curves used to quantify the metal
157 elements were obtained by using bulk reference materials. The resulting depth in the reference
158 materials was measured with a perthometer (PerthoConcept, Mahr Mesure). The crater depth
159 cartography in the stainless steel was measured using an optical interferometer (Bruker
160 ContourGT). A sample is also observed by Transmission Electron Microscopy (TEM), coupled
161 with an EDX detector. The instruments used are a Tecnai Osiris TEM and a ChemiSTEM EDX
162 detector, constructed both by FEI. The TEM characterizations are performed on a sample prepared
163 by Focused Ion Beam (FIB) on a Strata 400S FIB, constructed by FEI.

164 Three specimens are obtained after 122 h, six after 250 h and three after 500 h in the CorroNa
165 static sodium device. All the specimens are weighed before and after the corrosion test and
166 further characterized by GDOES. All the samples obtained after 250 and 500 h are observed by

167 SEM and analysed by EDX and DRX. One sample, immersed during 250 h is prepared by FIB
168 and observed by TEM.

169

170 **3. Experimental results highlighting corrosion processes**

171 Figure 2 gives the difference between the sample masses after and before immersion in liquid
172 sodium (positive in case of mass gain and negative in case of mass loss) versus time. The
173 formation of a solid product with impurities and/or sodium leads to a mass gain of the sample
174 while a dissolution phenomena leads to a mass loss. In the test presented here, the sample mass
175 increases after immersion in liquid sodium containing $189 \mu\text{g}\cdot\text{g}^{-1}$ of oxygen during 122 h. At
176 longer immersion time, the sample loses mass when the immersion time increases.

177

178 **3.1. Morphology and composition of the corrosion products**

179 The surface of a sample immersed during 250 h is shown in Fig. 3a. The surface features are
180 typical of the characterizations obtained in all conditions. Two morphologies are shown on the
181 sample surface, a dark one and a grey light one.

182 The sample surface is mainly covered with triangle-shaped crystals, rich in chromium, sodium
183 and oxygen (Fig. 3b, EDX analysis of the white cross in Fig. 3a). Iron, nickel and molybdenum
184 are also detected in this area, probably from the steel substrate. Considering the triangle shape [8]
185 combined with the elements detected by EDX and thermodynamic data [20], this phase might be
186 sodium chromite NaCrO_2 .

187 The clearer phase is rich in molybdenum and iron (Fig. 3c, EDX analysis of the black cross in
188 Fig. 3a). Chromium and nickel are also detected in this phase, probably from the steel substrate.

189

190 **3.2. Nature of the phases formed during corrosion**

191 The different phases described in Section 3.1 were characterized using XRD to determine their
192 chemical nature. The experimental XRD diagram, obtained for the steel sample immersed in
193 liquid sodium at 650°C for 500 h, was compared with the theoretical diagram of austenite,
194 NaCrO_2 and several M_6C carbides containing Cr, Mn, Fe, Ni and Mo (Fig. 4). The XRD
195 characterizations confirmed the formation of both sodium chromite (NaCrO_2) and M_6C carbides
196 for all the corrosion times. The closer carbide seems to be $\text{Fe}_3\text{Mo}_3\text{C}$. These characterizations
197 confirm the formation of sodium chromite previously characterized by SEM [13] and clarify the
198 nature of the molybdenum rich phase as M_6C , a molybdenum and iron rich carbide.

199

200 **3.3. In-depth corrosion**

201 **3.3.1. Cross-section observations**

202 The cross-section of a sample immersed in liquid sodium for 250 h at 650°C is shown in Fig. 5.
203 This SEM image is obtained in backscattered electron (BSE) mode, in which materials with
204 elements composed of higher atomic number (Z) appear clearer than the one with lower Z
205 elements.

206 At the top of the image, the mounting resin appears in black. At the bottom, the stainless steel
207 appears to be grey. A dark grey layer, corresponding to the sodium chromite layer, is observed

208 below the mounting resin. This sodium chromite layer seems to be discontinuous in some
209 locations. In between this oxide scale and the steel substrate, cavities (dark areas) are formed. In
210 addition, a lighter grey phase is seen between the Cr-Na-O-rich zone and the top of the cavity
211 zone. This phase might be molybdenum and iron rich carbide M_6C .

212 A grain boundary is visible in the middle of the cross-section. This grain boundary emerges at the
213 steel surface and was probably in contact with liquid sodium at the beginning of the corrosion
214 process. Its upper part is filled with oxide. A cavity is present immediately beneath oxide.

215

216 3.3.2 In-depth concentration profiles

217 The composition depth profiles of carbon, oxygen, chromium, iron, nickel, molybdenum and
218 sodium obtained through GDOES are plotted together in Figure 6. The element compositions in
219 log-scale are given as a function of depth for the sample corroded for 250 h at 650°C in liquid
220 sodium with an oxygen content of 189 $\mu\text{g}\cdot\text{g}^{-1}$. The origin of the x -axis corresponds to the
221 specimen surface. The maximum depth of 12 μm corresponds to the mean depth of the crater left
222 by the analysis. The scales of the two analyses (GDOES, fig. 6 and SEM, fig. 5) are not an exact
223 match: 5 μm in the SEM image corresponds to 4 μm in the composition depth profile. This slight
224 difference can be explained by the fact that the composition profiles measured through GDOES
225 are averaged over the 4 mm-diameter area analysed, whereas SEM provides a much more local
226 observation and by the fact that the erosion rate might be slightly different from one phase to the
227 other. In any case, as is shown below, the agreement between the two characterizations is
228 excellent. The different depths cited below are deduced from the GDOES profiles.

229 At the steel surface, the composition profiles indicate enrichment in oxygen, sodium and
230 chromium in a 1 μm -thick surface layer, corresponding to the sodium chromite scale (Figs. 4 and
231 5). It should be noted that the oxygen composition decreases whereas the sodium and chromium
232 compositions slightly increases in this oxide scale from the surface to the depth of 1 μm . The
233 iron, nickel and molybdenum compositions increase in the oxide scale from nearly 0.1 at.% at the
234 specimen surface to 8, 2 and 2 at.% respectively.

235 The composition profiles under the oxide scale differ from those of the bulk of the steel substrate.
236 The thus affected area corresponds to the presence of corrosion products (Fig. 4 and Fig. 5) and
237 can be divided into two zones. The first zone is located at depths between 1 μm and 1.55 μm
238 beneath the specimen surface. The compositions of molybdenum and carbon rise to a peak of 3.1
239 at.% and 0.38 at.% respectively at approximately 1.3 μm . These composition peaks correspond to
240 the Mo and Fe-rich carbides (light grey phase, Fig. 5). The Cr composition profile presents a
241 slightly depleted zone at around 1.55 μm . The evolution as a function of immersion time (less
242 than 500 h) of the location of the chromium minimum concentration could not be measured
243 because included in the measurement uncertainty ($\pm 0.2 \mu\text{m}$). The second zone is located at
244 depths ranging between 1.55 and 5.25 μm , with a slight increase in the Fe, Cr and Ni
245 compositions to their bulk values and a sharp decrease in the C, O and Na contents. The slope
246 changes in the sodium composition profile (inflexion points indicated by arrows in Fig. 6) are
247 consistent with the characteristic depth of internal oxides and cavities formed underneath at the
248 grain boundaries.

249 Under the affected area, no corrosion products are found in the steel substrate (Fig. 5). However,
250 the Na and O contents are not equal to zero and they decrease slightly to their detection limits.

251 This last segment of the composition profiles, plotted in Log-scale, must be considered with care
252 and could be an artefact of the GDOES measurements because the shape of the sputter crater
253 shows a steadily increasing deviation from its ideal shape upon increasing sputtering time.
254 Additionally, crater edge effects provide a more significant contribution to the overall signal
255 upon increasing crater depth.

256 In the end, it should be reminded that the experimental results described above were obtained for
257 different surface roughnesses, obtained by mechanical polishing stopped at different stages (1200
258 and 4000-grit SiC paper and 1 μm diamond suspension). Our tests demonstrated that the
259 corresponding surface roughnesses have no influence on the corrosion mechanisms studied.

260

261 **4. Chromium concentration evolution nearby the surface**

262 In the literature, it is demonstrated that oxygen strongly affects the behaviour of chromium by the
263 formation of NaCrO_2 [13-17]. That is why the evolution of chromium concentration was analysed
264 close to metallurgical defects such as grain boundaries (section 4.1). The mean chromium
265 concentration was also characterized as a function of immersion time (section 4.2).

266

267 **4.1. Evolution of chromium concentration along an emerging grain boundary**

268 Thin foils obtained by FIB are useful to measure the local elementary composition by EDX with
269 TEM. This experimental technique is used to characterize chromium composition around a grain
270 boundary.

271 The HAADF (High-Angle Annular Dark-Field) image of a sample immersed during 250 h in
272 liquid sodium containing $189 \mu\text{g}\cdot\text{g}^{-1}$ of oxygen at 650°C is presented in Fig. 7. The white layer at
273 the top of the image corresponds to a tungsten protecting layer deposited during FIB processing.
274 The dark grey layer below corresponds to the sodium chromite layer. The steel grain boundary is
275 highlighted by a dotted line. Some white spots, corresponding to M_6C carbides, are visible
276 between the metal and the sodium chromite layer. Cavities are not present on this part of the
277 sample.

278 The red arrows numbered “1” and “2” in Fig. 7 correspond to the location of the chromium EDX
279 analysis shown in Fig. 8. The chromium concentration is plotted as a function of distance from
280 the grain boundary (located at abscissa 0). The measurement length was 100 nm in the left steel
281 grain and 350 nm in the right steel grain. The chromium composition decreases from the center of
282 the grains to the grain boundary where it reaches a minimum. The concentration profile 1 exhibits
283 two Cr concentration peaks which might correspond to small phases rich in chromium such as
284 carbides or oxides.

285 Moreover, the chromium concentration of profile 1 is lower than the concentration of profile 2,
286 because the location of profile 1 is closer to the surface.

287 To summarize, the alloy is chromium-depleted around emerging grain boundary, and closer the
288 location is to the steel surface and the grain boundary, higher the chromium depletion is.

289

290 **4.2. Evolution of chromium depletion as a function of immersion time**

291 The mean chromium concentration profile measured by GDOES is given as a function of depth in
292 Fig. 9 for three immersion times in liquid sodium (122, 250 and 500 h). For all trials, the origin of
14

293 x -axis is placed at the minimum chromium concentration, assumed to be the interface between
294 steel and corrosion products as discussed before (section 3.3.2). At 10 μm depth at the most, the
295 Cr concentration of all samples reaches the initial concentration of the studied steel for the three
296 immersion times. In the following, this steel zone that is not affected by corrosion is called the
297 steel bulk.

298 At the interface between steel and corrosion products, the chromium concentration does not
299 depend on immersion time. From this interface to the bulk, the chromium concentration increases
300 in all cases. The lower chromium concentration is obtained for the samples immersed longer in
301 liquid sodium. The samples immersed during 500 h are more chromium depleted than the
302 samples immersed during 250 h which are also more depleted than the samples immersed during
303 122 h.

304

305 **5. Discussion**

306 In the following sections, a discussion is held concerning the final structure of the corrosion
307 products (Section 5.1) and the mechanisms explaining their formation (Section 5.2).

308 **5.1. Final structure of the corrosion products**

309 As shown in Section 3, during immersion in liquid sodium containing $189 \mu\text{g}\cdot\text{g}^{-1}$ of oxygen at
310 650°C , the stainless steel studied became covered with a sodium chromite (NaCrO_2) layer.
311 Molybdenum and iron rich carbides (M_6C) are also formed underneath. These observations
312 confirm previous results described in the literature, i.e. formation of sodium chromite [8, 12-16]
313 and carbides [9] in oxidizing and carburizing conditions.

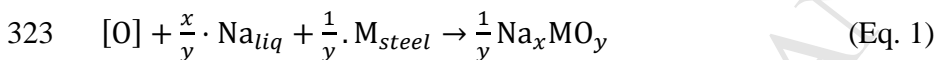
314 The system studied here is composed of liquid sodium containing traces of dissolved oxygen and
 315 carbon in contact with a stainless steel containing Cr, Fe and Mo. Thermodynamic calculations
 316 described below will show that NaCrO_2 and M_6C are equilibrium phases in such a system.

317

318 5.1.1. Oxides' stability

319 Three main solid oxides can be formed at the steel surface or in liquid sodium: sodium chromite
 320 (NaCrO_2), sodium ferrate (Na_4FeO_3) [21] and sodium oxide (Na_2O).

321 At the steel surface, the chemical reaction corresponding to solid Na_xMO_y formation can be
 322 written as follows:



324 where $\text{M}_{steel} = \text{Fe}$ or Cr in solid solution in steel, x and y are the stoichiometric coefficients of
 325 Na_xMO_y and $[\text{O}]$ corresponds to oxygen dissolved in liquid sodium.

326 The reference state is chosen to be pure liquid sodium, pure body-centered cubic solid M and
 327 pure O_2 at standard pressure of 1.013 bar. At thermodynamic equilibrium, the law of mass action
 328 is given by:

$$329 \quad \mu_{[\text{O}]} = \frac{1}{y} \cdot \left(\Delta G_{f, \text{Na}_x\text{MO}_y}^0 + RT \cdot \ln \frac{a_{\text{Na}_x\text{MO}_y}}{a_{\text{M}} \cdot a_{\text{Na}}^x} \right) \quad (\text{Eq. 2})$$

330 where $\mu_{[\text{O}]}$ is the chemical potential of oxygen in liquid sodium, $\Delta G_{f, \text{Na}_x\text{MO}_y}^0$ is the standard
 331 Gibbs free energy of formation of Na_xMO_y , R is the gas constant ($R = 8.314 \text{ J} \cdot \text{mol}^{-1} \cdot \text{K}^{-1}$), T is the
 332 temperature, $a_{\text{Na}_x\text{MO}_y}$, a_{M} and a_{Na} are the activities of Na_xMO_y , M and Na respectively.

333 As a first approximation, liquid sodium and the oxides formed can be considered to be pure, i.e.,
334 $a_{Na} = 1$ and $a_{Na_xMO_y} = 1$. The activities of Fe and Cr in austenite are calculated as a function of
335 temperature by means of the CALPHAD method implemented in ThermoCalc[®], with the TCFE8
336 (Steels/Fe-Alloys v8.0) database. For instance, at 650°C, $a_{Fe} = 0.67$ and $a_{Cr} = 0.28$, in using the
337 reference as pure stable metal (body-centered cubic for chromium and iron). The steel
338 composition used for the calculation is limited to the main elements (Cr, Ni, Mo, Mn, C, Si and
339 Fe). The contents of Cr, Ni, Mo, Mn, C and Si are the ones given in Table 1 and the balanced Fe
340 content is slightly higher than in the real stainless steel. This choice was made because the
341 calculation including the minor elements did not converge. With this choice, the activities of the
342 chosen elements are supposed to be weakly dependent on minor elements. This seems quite
343 reasonable for Cr and Fe which are the only ones considered for the oxides' formation ($NaCrO_2$
344 and Na_4FeO_3). The Cr and Fe contents are indeed much higher than those of the other elements.
345 The standard Gibbs free energy of formation (in $\text{kJ}\cdot\text{mol}^{-1}$) of $NaCrO_2$ ($-874.6 + 0.20921\cdot T$) and
346 Na_4FeO_3 ($-1214.17 + 0.34269\cdot T$) are given in Ref. [20] as a function of temperature T in K. The
347 relative stability of both oxides can be shown in the Ellingham diagram presented in Fig. 10a.
348 The chemical potential of oxygen in liquid sodium given by Eq. 2 is plotted as a function of
349 temperature for Na_4FeO_3 (purple line) and $NaCrO_2$ (blue line). The oxide is spontaneously
350 formed in the region above the corresponding straight line.

351 In liquid sodium, the chemical reaction corresponding to solid Na_2O formation can be written as
352 follows:



354 At thermodynamic equilibrium, the law of mass action leads to:

$$355 \quad \mu_{[O]} = \Delta G_{f,Na_2O}^0 + RT \cdot \ln \frac{a_{Na_2O}}{a_{Na}^2} \quad (\text{Eq. 4})$$

356 where $\Delta G_{f,Na_2O}^0$ ($= -421.5 + 0.1414 \cdot T$ in $\text{kJ} \cdot \text{mol}^{-1}$ [22]) is the standard Gibbs free energy of
 357 formation of Na_2O and $a_{Na} = 1$. If Na_2O is supposed to be pure, $a_{Na_2O} = 1$. In this case, the
 358 chemical potential of oxygen in liquid sodium given by Eq. 4 is represented by the black straight
 359 line in the Ellingham diagram (Fig. 10a). Na_2O is spontaneously formed in the region above this
 360 straight line.

361 The chemical potential of oxygen in liquid sodium must be calculated in the conditions studied
 362 here (i.e., $[O] = 189 \mu\text{g} \cdot \text{g}^{-1}$ and 650°C), in order to determine if the oxides considered above
 363 (Na_4FeO_3 , NaCrO_2 and Na_2O) are stable.

$$364 \quad \mu_{[O]} = R \cdot T \cdot \ln a_{[O]} \quad (\text{Eq. 5})$$

365 where $a_{[O]}$ is the activity of oxygen in liquid sodium, the reference state being pure O_2 at
 366 standard pressure of 1.013 bar. The solubility of oxygen in sodium $w_{[O]}^{Na,sat}$ can be found in the
 367 literature [23] ($\log w_{[O]}^{Na,sat} = 6.2571 - \frac{2444.5}{T}$ in $\mu\text{g} \cdot \text{g}^{-1}$). It can therefore be convenient to define
 368 the activity of oxygen in liquid sodium $a'_{[O]}$ with the reference state of liquid sodium saturated in
 369 oxygen (i.e., $a'_{[O]} = 1$ for oxygen-saturated liquid sodium).

370 Oxygen is present in small quantities in liquid sodium, in the form of a dilute solution (at 650°C ,
 371 $w_{[O]}^{Na,sat} = 0.4 \text{ wt.}\%$ or $x_{[O]}^{Na,sat} = 0.6 \text{ mol.}\%$). As currently done for oxygen in liquid iron [24],
 372 Henry's law can be used to express the activity of oxygen in liquid sodium:

$$373 \quad a'_{[O]} = \gamma_{[O]}^\circ \cdot x_{[O]} \quad (\text{Eq. 6})$$

374 where $\gamma_{[O]}^{\circ}$ is the Henry's law constant and $x_{[O]}$ the mole fraction of oxygen in liquid sodium.

375 Assuming that Henry's law is validated for oxygen content lower than or equal to its solubility in

376 liquid sodium:

$$377 \quad \gamma_{[O]}^{\circ} = \frac{1}{x_{[O]}^{Na,sat}} \quad (\text{Eq. 7})$$

378 and

$$379 \quad a'_{[O]} = \frac{x_{[O]}}{x_{[O]}^{Na,sat}} \quad (\text{Eq. 8})$$

380 As the oxygen content is low in liquid sodium, the activity of oxygen is also given by:

$$381 \quad a'_{[O]} = \frac{w_{[O]}}{w_{[O]}^{Na,sat}} \quad (\text{Eq. 9})$$

382 Finally,

$$383 \quad \mu_{[O]} = R.T. \ln a_{[O]} = R.T. \ln a'_{[O]} + \Delta G_{diss} \quad (\text{Eq. 10})$$

384 where ΔG_{diss} is the Gibbs free energy change for the chemical reaction



386 with $[O]_{Na_{liq}}^{sat}$ the oxygen dissolved in liquid sodium at saturation.

387 To our knowledge, there is no measurement of ΔG_{diss} in the literature. Fig. 10b represents the

388 Gibbs free energy of formation of Na-O binary phases as a function of mole fraction of oxygen

389 $x_{[O]}$ at a particular temperature T , the reference state being pure liquid sodium and pure O_2 gas.

390 The general case is schematized in blue. The Gibbs free energy of formation of Na-O liquid

391 phase is represented by the blue curve. The coordinates of the point corresponding to Na_2O are

392 $x_{[O]} = \frac{1}{3}$ and $\frac{1}{3} \cdot \Delta G_{f,Na_2O}^0$. When Na_2O is in equilibrium with the liquid phase, the point

393 corresponding to Na_2O belongs to the straight line tangent to the liquid phase curve at the
 394 composition $x_{[\text{O}]}^{\text{Na},\text{sat}}$. This tangent line cuts the $x_{[\text{O}]} = 1$ axis at the ordinate $R.T. \ln a_{[\text{O}]}^{\text{Na},\text{sat}}$, where
 395 $a_{[\text{O}]}^{\text{Na},\text{sat}}$ is the activity of oxygen in liquid sodium in equilibrium with Na_2O . This intersect also
 396 corresponds to the origin of the $a'_{[\text{O}]}$ scale (i.e., $R.T. \ln a'_{[\text{O}]} = 0$, Eq.8). The corresponding
 397 ΔG_{diss} is then given by Eq. 10 written in this particular case:

$$398 \quad \mu_{[\text{O}]} = R.T. \ln a_{[\text{O}]}^{\text{Na},\text{sat}} = \Delta G_{\text{diss}} \quad (\text{Eq. 12})$$

399 If the oxygen content $x_{[\text{O}]}$ in liquid Na is less than $x_{[\text{O}]}^{\text{Na},\text{sat}}$, the red tangent line (Fig. 10b) to the
 400 liquid phase curve cuts the $x_{[\text{O}]} = 1$ axis at the ordinate $R.T. \ln a_{[\text{O}]}$. The different terms of Eq. 10,
 401 in particular $R.T. \ln a'_{[\text{O}]}$, can be determined as shown in Fig. 10b.

402 The value of ΔG_{diss} depends on the shape of the Gibbs free energy of formation of Na-O liquid
 403 phase which is unknown. As oxygen is dissolved in liquid Na, $\Delta G_{\text{diss}} \leq 0$. Another limiting case
 404 is presented in Fig.10b, with the blue dashed line. It corresponds to the minimum value of the
 405 Gibbs free energy of formation of Na-O liquid phase at $x_{[\text{O}]}^{\text{Na},\text{sat}}$ and therefore the maximum value
 406 of ΔG_{diss} . Using Thales' theorem,

$$407 \quad \Delta G_{\text{diss}} > \Delta G_{f,\text{Na}_2\text{O}}^0 \quad (\text{Eq. 13})$$

408 Finally, with the real shape of the Gibbs free energy of formation of Na-O liquid phase,

$$409 \quad \Delta G_{f,\text{Na}_2\text{O}}^0 < \Delta G_{\text{diss}} < 0 \quad (\text{Eq. 14})$$

410 At 650°C , $-290988 < \Delta G_{\text{diss}} < 0$ (J mol^{-1}).

411 As liquid sodium is almost pure, the activity of Na in liquid sodium can be expressed by Raoult's
 412 law. With this assumption, the solid blue line described above cuts the $x_{[O]} = 0$ axis at the
 413 ordinate $R \cdot T \cdot \ln(1 - x_{[O]}^{Na,sat})$ and the $x_{[O]} = 1$ axis at the ordinate given by:

$$414 \mu_{[O]} = \Delta G_{f,Na_2O}^0 - 2 R \cdot T \cdot \ln(1 - x_{[O]}^{Na,sat}) = \Delta G_{diss} \quad (\text{Eq. 15})$$

415 For instance, at 650°C, the solid blue line cuts the $x_{[O]} = 0$ (resp. $x_{[O]} = 1$) axis at -45 J mol^{-1}
 416 (resp. $-290898 \text{ J mol}^{-1}$). Finally, ΔG_{diss} can be estimated by $\Delta G_{f,Na_2O}^0$ since the relative
 417 uncertainty induced by this approximation is less than 0.05% in the temperature range [400;
 418 700°C]. This means that the tangent line to the liquid phase curve at the composition $x_{[O]}^{Na,sat}$ is close
 419 to the blue dashed line.

420 In Fig. 10a, $\mu_{[O]} = R \cdot T \cdot \ln a_{[O]}$ (Eq. 10) is plotted for different oxygen contents in liquid sodium
 421 and $\Delta G_{diss} = \Delta G_{f,Na_2O}^0$. Let us first consider the curve corresponding to an oxygen content of
 422 $1000 \mu\text{g}\cdot\text{g}^{-1}$. The calculation predicts that solid Na_2O is in equilibrium with liquid sodium
 423 containing $1000 \mu\text{g}\cdot\text{g}^{-1}$ for temperatures less than 751 K. This is in good agreement with
 424 measurements found in the literature [23]. This means that the unknown value ΔG_{diss} can be
 425 approximated by $\Delta G_{f,Na_2O}^0$ (as was done before [21]). For an oxygen concentration of $189 \mu\text{g}\cdot\text{g}^{-1}$
 426 in liquid sodium (red $\mu_{[O]}$ curve, Fig. 10a), at temperatures higher than 350°C, the chemical
 427 potential of oxygen is lower than the one required to form Na_2O or Na_4FeO_3 and higher than the
 428 one required to form NaCrO_2 . It implies that in our experimental conditions, i.e., 650 °C and
 429 $189 \mu\text{g}\cdot\text{g}^{-1}$ of oxygen, the sodium chromite formation is thermodynamically possible while the
 430 formation of sodium oxide and sodium ferrate is not possible.

431

432 5.1.2. Carbides' stability

433 The carbides' stability is also investigated by means of ThermoCalc[®] based on CALPHAD
434 method, with the TCFE8 (Steels/Fe-Alloys v8.0) database. As for the calculations of the oxides'
435 stability, the steel composition is limited to the main elements in austenite (Cr, Ni, Mo, Mn, C, Si
436 with the contents given in Table 1 and Fe with a content slightly higher than in the real stainless
437 steel). The carbides considered are $M_{23}C_6$, M_3C_2 , M_5C_2 , M_6C , M_7C_3 , where M can be Cr, Mn, Fe,
438 Ni and Mo. The activity of the elements in austenite in equilibrium with carbides is essentially
439 unchanged (lower than 1 hundredth) compared to the activity of the elements in austenite (used in
440 section 5.1.1).

441 Fig. 11a gives the results of the mole fraction of stable phases as a function of temperature. The
442 mole fraction of austenite is closed to 1 for all temperatures. The most stable carbide is M_6C for
443 temperatures below 615 °C ($M_{23}C_6$ also exists but at a very low molar fraction less than 10^{-3}) and
444 $M_{23}C_6$ for temperatures higher than 650 °C (together with M_6C at a very low molar fraction). In
445 between, both carbides are present. Fig. 11b and Fig. 11c present the elemental composition of
446 M_6C and $M_{23}C_6$ carbides. M_6C carbides contain mainly Mo, Fe and C and $M_{23}C_6$ carbides mainly
447 Cr and C. At 650°C, the carbides formed in the stainless steel studied here are rich in Mo and the
448 XRD peaks are consistent with M_6C carbides containing mainly Mo, Fe and C (such as Fe_3Mo_3C)
449 and in small proportions Cr, Mn and Ni. At 650 °C, the M_6C composition given by
450 thermodynamic calculations is close to Mo_4Fe_2C (Fig. 11b) (Mo: 48 at.%, Fe: 29.3 at.%, C: 14.3
451 at.%, Cr: 8 at.%). It can therefore be concluded that the M_6C carbides formed are in
452 thermodynamic equilibrium in the system, even if the calculated maximum temperature for M_6C

453 stability is less than 650 °C (Fig. 11a). This temperature could be slightly underestimated by the
454 calculations.

455

456 **5.2. Mechanisms and driving forces of corrosion phenomena**

457 Corrosion tests in liquid sodium containing 189 $\mu\text{g}\cdot\text{g}^{-1}$ of oxygen at 650°C pointed out the
458 formation of corrosion products composed of sodium chromite NaCrO_2 and M_6C carbides
459 containing Mo and Fe (Fig. 4). The observation of cross sections showed that cavities are formed
460 between these corrosion products and the stainless steel (Fig. 5). Finally, a dissolution of the
461 stainless steel is highlighted by the mass loss measured for immersion durations of 250 and 500 h
462 (Fig. 2).

463 The oxidation and carburization mechanisms are described in Section 5.2.1, the dissolution driving
464 forces in Section 5.2.2 and the cavities formation mechanisms in Section 5.2.3..

465

466 **5.2.1. Oxidation and carburization mechanisms**

467 *Selective oxidation*

468 The stainless steel surface under study became covered with a NaCrO_2 scale during immersion in
469 liquid sodium. This is a selective oxidation phenomenon, chiefly external, i.e. it occurs on the
470 stainless steel surface (Fig. 5). From a depth of 10 μm and moving towards the steel surface, the
471 general shape of the chromium profiles exhibit an initial, constant concentration zone that
472 corresponds to the concentration in the stainless steel bulk then a concentration decrease down to
473 minimum concentration (depletion zone) and, finally, an increase in concentration towards the

474 surface (Fig. 9). The concentration profiles obtained are the result of Cr selective oxidation with
475 Cr diffusion from the steel bulk to the NaCrO_2 / steel interface (depth = 0, Fig. 9) and NaCrO_2
476 formation on the steel surface (depth < 1 μm , Fig. 9). The minimum Cr concentration remains
477 more or less constant at approximately 12 ± 1 at.% from 122 to 500 h (average and uncertainty
478 on all specimen). This concentration could correspond to Cr concentration in the stainless steel at
479 equilibrium with NaCrO_2 . However, caution should be exercised with the conclusion about this
480 particular issue, as a rough thermodynamic assessment would rather give a Cr concentration in
481 equilibrium with NaCrO_2 close to the null value [28] and precise experimental data are still
482 lacking. Indeed, it should be mentioned that the measurement of the Cr concentration by GDOES
483 probably lacks of accuracy. This is a mean Cr concentration measured by sputtering the elements
484 in a 4 mm diameter crater with the contribution of the different corrosion products. For instance,
485 tiny carbides (Fig. 8) contribute as well to the Cr concentration.

486 In Fig. 9, the shape of Cr concentration profiles is characteristic of diffusion in polycrystalline
487 materials [25-28], with the influence of the presence of grain boundaries (e.g., from 1.6 to 4.6 μm
488 at 500°C). This is confirmed by the Cr concentration profiles measured in the vicinity of grain
489 boundaries (Fig. 8). Cr depletion is larger in the grain boundary than in the adjacent grains. This
490 result indicates that the Cr diffusion coefficient is higher in the grain boundary than in the grain
491 (grain boundaries are known to be diffusion short-circuits [32]). In Fig.8, the local Cr
492 concentration decreases from the steel bulk (profile 2) to the surface (profile 1). This is in good
493 agreement with the mean Cr concentration profiles measured by GDOES as described just before.
494 Finally, NaCrO_2 is formed by the reaction of chromium diffusing from the steel bulk with two
495 components of liquid metal, namely sodium and dissolved oxygen. The oxidation front can be

496 located either at the NaCrO_2 / steel interface or NaCrO_2 / liquid metal interface. The experiments
497 presented here do not show where the oxidation front is located. Some prior results at 550°C are
498 reported in the literature [28], indicating an inner oxidation front.

499

500 *Carbides formation*

501 M_6C carbides rich in Fe and Mo were present in between the NaCrO_2 scale and the stainless steel
502 after immersion in liquid sodium (Fig. 5). Mo segregates to the steel surface where it reacts with
503 Fe from the steel and dissolved C present in liquid sodium. The experimental conditions of the
504 test were already observed as carburizing for this low carbon steel [18], probably because of high
505 carbon content due to the fabrication process of the sodium metal. Carbon diffuses into the steel
506 matrix and precipitates into carbides representative of the local composition : Mo rich carbide
507 (peak at $1.5\ \mu\text{m}$ in Fig. 6), or Fe-Cr rich carbides (peak at $2.8\ \mu\text{m}$ in Fig. 6). The Mo
508 concentration profiles obtained present a slight depletion zone (around $2\ \mu\text{m}$ in Fig. 6), due to the
509 formation of Mo rich carbides. Carbides could be formed before, at the same time or after
510 NaCrO_2 . As they were detected under NaCrO_2 for all corrosion times investigated, it is not
511 possible to deduce from the experiments where the carburization front is located

512

513 **5.2.2. Driving force of dissolution**

514 It was shown that the mass of the stainless steel samples decreased during immersion in liquid
515 sodium for 250 and 500 h (Fig. 2). This means that the stainless steel substrate and / or the
516 chromite scale are dissolved in parallel with the formation of chromite and carbides. The
517 dissolution of the main elements of stainless steel, namely Fe, Ni, Cr and Mn, was already
25

518 reported to occur in liquid sodium, mainly at low oxygen levels (section 1) [4-7]. The Fe and Ni
 519 depletion observed at the metal / oxide interface (Fig. 6) is due to their dissolution in liquid
 520 sodium.

521 Considering the principal elements in the stainless steel chosen (table 1), the driving force of
 522 dissolution is a function of the Fe, Cr, Ni, Mn and Mo concentrations in liquid sodium at
 523 equilibrium with steel:

$$524 \quad M_{steel} \leftrightarrow M_{Na} \quad (\text{Eq. 16})$$

525 where M_{steel} means M in solid solution in steel and M_{Na} is M dissolved in liquid sodium, M
 526 being Fe, Cr, Ni, Mn or Mo. These equilibrium concentrations can be estimated using the
 527 solubility of the elements in liquid sodium and their activities in the steel if one assumes that the
 528 solubility of one dissolved element does not change in presence of the others (we made this
 529 strong assumption because of a lack of more precise data). The solubility of M in sodium
 530 $w_M^{Na,sat}$ (in $\mu\text{g}\cdot\text{g}^{-1}$) can be found in the literature (Fe [11], Cr [10], Ni [30], Mn [29] and Mo
 531 [19]). The solubility of M is defined as the M concentration in liquid sodium at equilibrium with
 532 pure stable solid M (body-centered cubic Fe, Cr, Mn and Mo, face-centered cubic Ni at 650°C).

533 At 650°C, $w_{Fe}^{Na,sat} = 1.9 \mu\text{g}\cdot\text{g}^{-1}$, $w_{Cr}^{Na,sat} = 0.41 \mu\text{g}\cdot\text{g}^{-1}$, $w_{Ni}^{Na,sat} = 2.4 \mu\text{g}\cdot\text{g}^{-1}$, $w_{Mn}^{Na,sat} = 1.4 \mu\text{g}\cdot\text{g}^{-1}$
 534 and $w_{Mo}^{Na,sat} = 2.3 \mu\text{g}\cdot\text{g}^{-1}$. As in section 5.1.1., the activities of Fe, Cr, Ni, Mn and Mo in austenite
 535 were calculated by means of the CALPHAD method in ThermoCalc[®] with the TCFE8 database.
 536 At 650°C, $a_{Fe} = 0.67$, $a_{Cr} = 0.28$, $a_{Ni} = 0.054$, $a_{Mn} = 0.0043$ and $a_{Mo} = 0.067$, the reference
 537 being pure stable metals.

538 M is present in small quantity in liquid sodium. As currently done in liquid iron [24], Henry's law
 539 can be used to express the activity of M in liquid sodium:

$$540 \quad a_M^{\text{Na}} = \gamma_M \cdot x_M^{\text{Na}} \quad (\text{Eq. 17})$$

541 where γ_M is the Henry's law constant for M and x_M^{Na} is the mole fraction of M in liquid sodium.

542 Assuming that Henry's law is valid for M content lower than or equal to its solubility in liquid

543 sodium, the following equation can be written based on the definition of solubility reminded

544 before (equilibrium between liquid sodium containing the M mole fraction $x_M^{\text{Na},sat}$ and pure M):

$$545 \quad \gamma_M \cdot x_M^{\text{Na},sat} = 1 \quad (\text{Eq. 18})$$

$$546 \quad \text{And therefore } a_M^{\text{Na}} = \frac{x_M^{\text{Na}}}{x_M^{\text{Na},sat}} \quad (\text{Eq. 19})$$

547 As the M content in liquid sodium is low, the activity of M in liquid sodium is also given by:

$$548 \quad a_M^{\text{Na}} = \frac{w_M^{\text{Na}}}{w_M^{\text{Na},sat}} \quad (\text{Eq. 20})$$

549 Finally, the equilibrium between stainless steel and liquid sodium leads to:

$$550 \quad a_M = a_M^{\text{Na}} = \frac{w_M^{\text{Na}}}{w_M^{\text{Na},sat}} \quad (\text{Eq. 21})$$

551 Based on this result, the maximum theoretical mass dissolved in liquid sodium (section 2.2) in the

552 CorroNa device is:

$$553 \quad \max(M_{dissolved}^{\text{Na}}) = \sum_M \frac{M_{\text{Na}} \cdot w_M^{\text{Na},sat} \cdot a_M}{N_{\text{samples}} \cdot s_{\text{sample}}} \quad (\text{Eq. 22})$$

554 where M_{Na} is the sodium mass contained in the CorroNa crucible (2.3 kg), N_{samples} is the

555 number of samples immersed in liquid sodium at the same time (6) and s_{sample} the sample

556 surface area (0.12 dm^2 for 2 faces). For the experiments performed here, it corresponds to 4.5
557 mg.dm^{-2} .

558 This theoretical mass loss is in good agreement with the one obtained after 250 h of immersion.
559 However, it is twice less than the one measured for samples immersed for 500 h. The data used to
560 determine the solubilities of each element (Fe [11], Cr [10], Ni [30], Mn [29] and Mo [19]) were
561 proposed for pure metals in pure sodium. In our case, oxygen is present in sodium and might
562 have modified these solubilities as suggested for chromium [19] and iron [4, 10, 11]. The
563 solubilities of chromium and iron are higher in sodium containing oxygen than in pure sodium
564 because some oxides are formed (NaCrO_2 , Na_4FeO_3). Therefore, the stainless steel under
565 investigation might be dissolved in sodium more than the value calculated above. Consequently,
566 the mass loss measured here is higher than expected in pure sodium.

567

568 **5.2.3. Cavities formation**

569 In our experiments of corrosion in liquid sodium, cavities were observed at the interface between
570 steel and NaCrO_2 scale (Fig. 5).

571 It is well known that an oxide scale growth at high temperature is sometimes accompanied by a
572 void formation within the metal [31-33]. In such a system, vacancies are created in the metal and
573 the vacancy supersaturation can lead to void formation by nucleation mainly on singularities such
574 as grain boundaries or interfaces. If vacancies are all annihilated at sinks like dislocations, they
575 do not cause void formation within the metal and the oxide / metal interface will translate to
576 consume the metal. Two sources of vacancies are described in the literature. First, the removal of
577 cations from the metal due to the growth of the oxide scale creates cationic vacancies at the

578 oxide / metal interface. Secondly, vacancies can also be created by the so-called Kirkendall
 579 effect: when the diffusivities of the different elements in the metal are different from each other, a
 580 vacancy flux is obtained in the opposite direction of the flux of the fastest element. This
 581 Kirkendall vacancy flux is oriented from the metal / oxide interface to the metal bulk (resp. from
 582 the metal bulk to the metal / oxide interface) when the selective oxidized element is the fastest
 583 (resp. the slowest) diffusing species in the alloy, leading to pores formation in the bulk of the
 584 alloy (resp. under the oxide scale). This is the case of high temperature oxidation of Ni-Cr alloys
 585 forming chromia scales in which Cr diffuses much faster than Ni [34] (resp. Ni-Al with
 586 Al < 50mol.%, forming Al₂O₃ scales in which Al diffuses slower than Ni [35]).
 587 In the case studied here, vacancies are created at the steel / NaCrO₂ interface by Cr oxidation,
 588 carburization (Section 5.2.1) and dissolution of the other elements present in the stainless steel
 589 (Section 5.2.2). The vacancies become supersaturated and this leads to the nucleation of the
 590 cavities observed (Fig. 5).

591 In the cross section presented in Fig. 5 (which is representative of the whole sample), the large
 592 cavities are 11.5 μm apart from each other. This can be used to estimate the surface density of
 593 cavities ($f_{cavities} = 7.6 \cdot 10^{-3} \mu\text{m}^{-2}$). Assuming that cavities are only due to chromium departure, the
 594 thickness of NaCrO₂ formed with the chromium creating the cavities is then given by:

$$595 \quad e_{\text{NaCrO}_2} = V_{\text{cavity}} f_{\text{cavities}} \frac{\rho_{\text{Cr}}}{\rho_{\text{NaCrO}_2}} \frac{M_{\text{NaCrO}_2}}{M_{\text{Cr}}} \quad (\text{Eq. 23})$$

596 where V_{cavity} is the mean volume of a cavity supposed to be spherical ($7.2 \mu\text{m}^3$), ρ_{Cr} the
 597 chromium density ($7150 \text{ kg}\cdot\text{m}^{-3}$ [36]), ρ_{NaCrO_2} the NaCrO₂ density ($4360 \text{ kg}\cdot\text{m}^{-3}$ [PDF-2/Release
 598 2012 RDB 04-010-6761]), M_{NaCrO_2} and M_{Cr} the NaCrO₂ and Cr molar masses (107 and 52 g.mol⁻¹

599 ¹ [36]), w_{Cr} the Cr mass fraction in the stainless steel studied (0.179, Table 1). Finally, the oxide
600 thickness estimated from the mean cavities volume is 0.2 μm after 250 h immersion. As shown in
601 Figs. 5 and 6, the measured oxide thickness is closed to 1 μm . As a consequence, it can be
602 deduced that the cavities' formation can result from selective oxidation of chromium into sodium
603 chromite. Even if the order of magnitude of the calculated thickness is rough, it can also be said
604 that 1) part of the vacancies created by Cr oxidation or steel dissolution is annihilated at sinks like
605 dislocations leading to the translation of the oxide / metal interface towards the metal bulk and 2)
606 the Kirkendall vacancy flux if it exists is not the main mechanism to explain the cavities
607 formation.

608

609 **6. Conclusions**

610 The corrosion of an austenitic steel in liquid sodium was investigated in this study. The austenitic
611 steel samples were immersed for 122, 250 and 500 h in liquid sodium with an oxygen content of
612 189 $\mu\text{g.g}^{-1}$ at 650°C. The steel samples were then characterized by means of complementary
613 techniques, namely scanning electron microscopy, X-ray diffraction, glow discharge optical
614 emission spectroscopy and transmission electron microscopy.

615 The characterizations showed the formation of a NaCrO_2 oxide scale at the steel surface together
616 with underlying M_6C carbide particles rich in molybdenum and iron. The stainless steel substrate
617 and / or the chromite scale were dissolved in parallel with the formation of chromite and carbides.
618 Cavities were observed under the oxide scale within the metal.

619 The system studied here is composed of liquid sodium containing traces of dissolved oxygen and
620 carbon in contact with a stainless steel. Thermodynamic calculations showed that NaCrO_2 and
621 M_6C are equilibrium phases in such a system.

622 NaCrO_2 is formed by the reaction of chromium diffusing from the steel bulk with two
623 components of liquid metal, namely sodium and dissolved oxygen. The Cr composition profiles
624 exhibited a depleted zone due to the formation of NaCrO_2 . This is a selective oxidation
625 phenomenon, chiefly external, i.e. it occurs on the stainless steel surface. Mo segregates to the
626 steel surface where it reacts with Fe from the steel and C dissolved in liquid sodium that diffuses
627 into the steel matrix according to a carburisation phenomenon.

628 Stainless steel and liquid sodium are not in thermodynamic equilibrium. The dissolution of
629 stainless steel occurred since the liquid sodium bath is not saturated in the dissolving species.
630 Thermodynamic calculations, using only the solubilities of Fe, Cr, Ni, Mn and Mo proposed in
631 the literature for pure metals in liquid sodium, did not explain the large amount of dissolved steel.
632 This means that the solubilities of these elements are higher in sodium containing oxygen than in
633 pure sodium. One explanation could be that some oxides, such as NaCrO_2 or Na_4FeO_3 , are
634 formed in liquid sodium, increasing the driving force of dissolution.

635 As for the cavities, vacancies are created at the steel / NaCrO_2 interface by Cr oxidation,
636 carburization and dissolution of the other elements present in the stainless steel. The vacancies
637 become supersaturated and this leads to the nucleation of the cavities observed. Part of the
638 vacancies created by Cr oxidation or steel dissolution is annihilated at sinks like dislocations
639 leading to the translation of the oxide / metal interface towards the metal bulk.

640 All of this still needs to be elucidated with additional experimental support

641

642 **7. Acknowledgements**

643 The authors are extremely grateful to Jean-Bernard Guillot for fruitful discussions, to the CEA-
644 Generation 4 / Structural material project for part of the financial support, to V. Lorentz for the
645 exposure of the specimen to liquid sodium made in the Corrona-1 test Bench of the CEA-Saclay.

646

647 **References**

648 [1] R. Daustray, Y. Bréchet, J. Friedel, Les fluides caloporteurs pour neutrons rapides, Académie
649 des sciences, EDPscience, Les Ulis, 2014.

650 [2] J.L. Courouau, F. Balbaud-Célérier, V. Lorentz, T. Dufrenoy, Corrosion by liquid sodium of
651 materials for sodium fast reactors: the CORRONa testing device, in: the proceedings of the
652 International Congress on Advances in Nuclear Power Plants (ICAPP '11), paper 11152, Nice,
653 France, May 2-5, 2011.

654 [3] P. Baqué, L. Champeix, A. Lafon, E. Sermet, Some aspects of corrosion of austenitic steels in
655 flowing sodium, in: Liquid Alkali Metals Proceedings of the International Conference Organized
656 by the British Nuclear Energy Society, Nottingham University, 1973, April 4-6, The British
657 Nuclear Energy Society, London, 1973, pp. 223-231

658 [4] J.R. Weeks, H.S. Isaacs, Corrosion and deposition of steels and nickel-base alloys in liquid
659 sodium, in: Advances in corrosion science and technology, vol. 3, Plenum Press, New York,
660 London, 1973, pp. 1-66.

- 661 [5] T. Suzuki, I. Mutoh, T. Yagi, Y. Ikenaga, Sodium corrosion behavior of austenitic alloys and
662 selective dissolution of chromium and nickel, *J. Nucl. Mater.* 139 (1986) 97-105.
- 663 [6] T. Gnanasekaran, R.K. Dayal, Liquid metal corrosion in nuclear reactor and accelerator
664 driven systems, in: D. Féron (Ed.), *Nuclear Corrosion Science and Engineering*, Woodhead
665 Publishing Limited – Cambridge, Philadelphia, 2012, pp.301-328.
- 666 [7] E. Yoshida, T. Furukawa, Corrosion issues in sodium-cooled fast reactor (SRF) systems, in:
667 D. Féron (Ed.), *Nuclear Corrosion Science and Engineering*, Woodhead Publishing Limited –
668 Cambridge, Philadelphia, 2012, pp.773-806.
- 669 [8] B.H. Kolster, Mechanism of Fe and Cr transport by liquid sodium un non-isothermal loop
670 system, *J. Nucl. Mater.* 55 (1975) 155-168.
- 671 [9] A.W. Thorley, J.A. Bradsley, Structural changes in materials exposed to liquid sodium, *J. R.*
672 *Microsc. Soc.* 88 (1968) 431-447.
- 673 [10] R.M. Singer, A.H. Fleitman, J.R. Weeks, H.S. Isaacs, Measurements of the solubility of iron
674 and chromium in sodium, in: *Corrosion by Liquid Metals, Proceedings of the sessions on*
675 *corrosion by liquid Metals of the 1969 fall meeting of the metallurgical society of AIM, October*
676 *13-16, 1969, Philadelphia, Pennsylvania, New-York – London: Plenum Press 1970, pp. 561-576.*
- 677 [11] W.P. Stanaway, R. Thompson, Solubility of metals, iron and manganese in sodium, in:
678 *Second international Conference on liquid metal technology in energy production – Proceedings*
679 *part 2, April 20-24, 198, Richland, Washington, J.M. Dahlke 1980, pp. 18.54-18.61.*
- 680 [12] B.H. Kolster, L. Bos, Sodium corrosion in a total molybdenum loop system: construction,
681 experience and results, in: *Liquid metal engineering and technology*, London: The British
682 Nuclear Energy Society 1984, pp.235-242.

- 683 [13] I.W. Cavell, M.G. Nicholas, Some observations concerned with the formation of sodium
684 chromite on AISI 316 exposed to oxygenated sodium, *J. Nucl. Mater.* 95 (1980) 129-144.
- 685 [14] A.G. Crouch, P.R. Bussey, Corrosion of ferritic steels in flowing sodium, in: *Ferritic steels*
686 *for fast reactor steam generators*, The British Nuclear Energy Society, London, 1978, 258-263.
- 687 [15] A.G. Crouch, The growth and stability of sodium chromite and its influence on corrosion, in:
688 J.M. Dahlke (Ed.), *Proceedings of the Second International Conference on Liquid Metal*
689 *Technology in Energy Production*, part 1, April 20-24, 1980, Richland, Washington, 1980, pp. 3-
690 43 to 3-51.
- 691 [16] S.H. Shin, J. Lee, J.H. Kim; J.H. Kim, Mechanism of corrosion of 9Cr and 12Cr
692 ferritic/martensitic steels under oxygen-saturated sodium, *Corr. Sci.* 2016.
693 <http://dx.doi.org/10.1016/j.corsci.2016.09.001>.
- 694 [17] P.L.F. Rademakers, B.H. Kolster, Corrosion of various ferritic steels in an isothermal
695 sodium loop system, *J. Nucl. Mater.* 97 (1981) 309-318.
- 696 [18] J.L. Courouau, V. Lorentz, M. Tabarant, S. Bosonnet, F. Balbaud-Célérier, Corrosion by
697 oxidation and carburization in liquid sodium at 550°C of austenitic steels for sodium fast
698 reactors, in: *Proceeding of International Conference on Fast Reactors and related fuel cycles: safe*
699 *technologies and sustainable scenarios (FR13)*, 4-7 march 2013, Paris, France.
- 700 [19] H.U. Borgsted, C.K. Mathews, *Applied chemistry of the alkali metals*, New-York: Plenum
701 Press, 1987, p.191 and p.184.
- 702 [20] B.J. Shaiu, P.C.S. Wu, P. Chiotti, Thermodynamic properties of the double oxide of Na₂O
703 with the oxides of Cr, Ni and Fe, *J. Nucl. Mater.* 67 (1977) 13-23.

- 704 [21] N.P. Bhat, H.U. Borgstedt, Corrosion behaviour of structural materials in sodium influenced
705 by formation of ternary oxides, *Werkstoffe und Korrosion* 39 (1988) 115-123.
- 706 [22] D.R. Fredrickson, M.G. Chasanov, The enthalpy of sodium oxide Na_2O to 1300 K by drop
707 calorimetry, *J. Chem. Thermodyn.* 5 (1973) 485-490.
- 708 [23] J.D. Noden, A general equation for the solubility of oxygen in liquid sodium, *Journal of the*
709 *British Nuclear Energy* 12-1 (1973) 57-62 and 329-331.
- 710 [24] A. Rist, M.-F. Ancey-Moret, C. Gatellier, P.-V. Riboud, Équilibres thermodynamiques en
711 sidérurgie, *Techniques de l'Ingénieur*, M 1730 (1974) 1-33 (in French).
- 712 [25] A.D. Le Claire, The analysis of grain boundary diffusion measurements, *Br. J. Appl. Phys.*
713 14 (1963) 351-366.
- 714 [26] I. Kaur, Y. Mishin, W. Gust, *Fundamentals of grain and interphase boundary diffusion*,
715 Wiley, Chichester, 1995.
- 716 [27] H. Mehrer, *Diffusion in solids*, in: M. Cardona, P. Fulde, K. von Klitzing, H.-J. Queisser, R.
717 Merlin, H. Störmer (Eds.), *Springer series in solid-state sciences*, Springer, Berlin, 2007.
- 718 [28] M. Rivollier, *Corrosion des aciers austénitiques par le sodium liquide en présence*
719 *d'oxygène*, PhD Thesis, CentraleSupélec, 2017 (in French).
- 720 [29] W.P. Stanaway et R. Thompson, « The solubility of transition metals, Mn and Co in liquid
721 sodium », in *Material behavior and physical chemistry in liquid metal system*, New York –
722 London: Plenum Press, H.U. Borgstedt 1982, 421-427.
- 723 [30] S.P. Awasthi, H.U. Borgstedt, An assessment of solubility of some transition metals (Fe, Ni,
724 Mn and Cr) in liquid sodium, *J. Nucl. Mater.* 116 (1983) 103-111.

- 725 [31] H.E. Evans, Cavity formation and metallurgical changes induced by growth of oxide scales,
726 J. Mater. Sci. Technol. 4 (1988) 1089-1098.
- 727 [32] D.J. Young, High Temperature Oxidation and Corrosion of Metals, Elsevier, Amsterdam,
728 2008.
- 729 [33] C. Desgranges, F. Lequien, E. Aublant, M. Nastar, D. Monceau, Depletion and voids
730 formation in the substrate during high temperature oxidation of Ni-Cr alloys, Oxid. Met. 79
731 (2013) 93-105.
- 732 [34] E. Schmucker, C. Petitjean, L. Martinelli, P.-J. Panteix, B. Lagha, M. Vilasi, Oxidation of
733 Ni-Cr alloy at intermediate oxygen pressures. II. Towards the lifetime prediction of alloys, Corr.
734 Sci. 111 (2016) 467–473.
- 735 [35] M.W. Brumm, H.J. Grabke, Oxidation behaviour of Ni-Al – II. Cavity formation beneath the
736 oxide scale on NiAl of different stoichiometries, Corros. Sci. 34 (1993) 547-561.
- 737 [36] David R. Lide, CRC Handbook of Chemistry and Physics, CRC Press Inc, 2009, 90th ed.,
738 2804 p., (ISBN 978-1-420-09084-0).

739

740 Legends

741 **Table 1.** Composition in wt.% of the 316L(N) stainless steel tested.

742 **Figure 1.** 316L(N) steel microstructure after electrochemical etching (oxalic acid, 10 vol.%, 0.5
743 A.cm⁻²).

744 **Figure 2.** Mass gain or loss of samples immersed at 650°C in liquid sodium containing an
745 oxygen content of 189 µg.g⁻¹ as a function of time.

746 **Figure 3.** Sample immersed for 250 h at 650°C in liquid sodium containing an oxygen content of
747 189 $\mu\text{g.g}^{-1}$, a) SEM observation in secondary electrons at 2 kV and associated b) and c) EDS
748 spectra); The steel surface is covered with a layer of triangle-shaped crystals rich in Na, Cr and
749 O. Mo and Fe rich particles are also detected.

750 **Figure 4.** XRD diagram, specimen immersed for 500 h at 650°C in liquid sodium containing
751 189 $\mu\text{g.g}^{-1}$ oxygen. NaCrO_2 and $\text{Fe}_3\text{Mo}_3\text{C}$ are identified together with the austenite substrate.

752 **Figure 5.** SEM cross-section observations (backscattered electrons); sample immersed for 250 h
753 at 650°C in liquid sodium with a 189 $\mu\text{g.g}^{-1}$ oxygen content.

754 **Figure 6.** GDOES chemical depth profiles obtained for a sample immersed in liquid sodium for
755 250 h at 650°C with an oxygen content of 189 $\mu\text{g.g}^{-1}$.

756 **Figure 7.** Cross section of a sample immersed for 250 h at 650°C in liquid sodium with 189 $\mu\text{g.g}^{-1}$
757 $\mu\text{g.g}^{-1}$ of oxygen (HAADF image). The NaCrO_2 scale is visible at the top of the image in black.

758 **Figure 8.** Chromium composition profile obtained by EDX analysis at the locations shown by
759 arrows 1 and 2 in Fig. 7. Abscissa 0 corresponds to the location of the grain boundary where a
760 chromium depletion is observed.

761 **Figure 9.** Chromium composition profile obtained by GDOES analysis for samples immersed
762 during 122, 250 and 500 h at 650°C in liquid sodium containing 189 $\mu\text{g.g}^{-1}$ of oxygen.

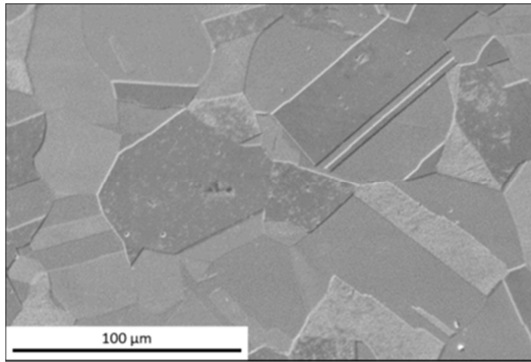
763 **Figure 10.** Oxides' stability: a) Ellingham diagram of NaCrO_2 , Na_4FeO_3 and Na_2O plotted
764 together with the chemical potential of oxygen for different oxygen contents in liquid sodium; b)
765 Gibbs free energy diagram for the equilibrium between Na-O liquid phase and Na_2O .

766 **Figure 11.** Carbides' stability: a) mole fraction of stable phases, b) Composition of M_6C carbide
767 as a function of temperature and c) Composition of $M_{23}C_6$ carbide as a function of temperature.
768

1 **Table 1.**

Fe	Cr	Ni	Mo	Mn	C	Si	P	S	Ti	Al	Cu	Co
Balanced	17.9	12.1	2.35	1.72	0.012	0.45	0.034	0.025	0.0015	0.0025	0.0025	0.0008

2



ACCEPTED MANUSCRIPT

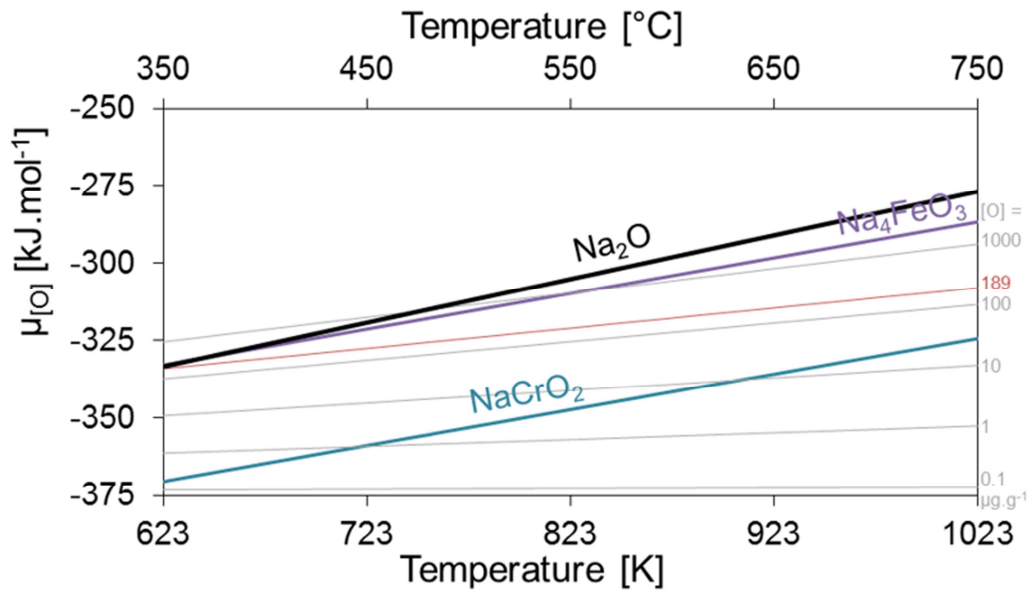


Fig.10a

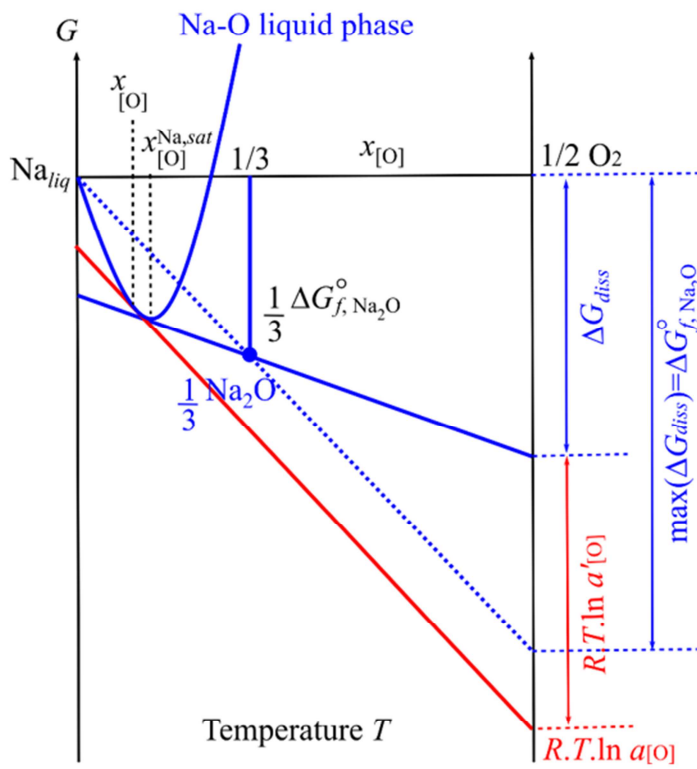


Fig.10b

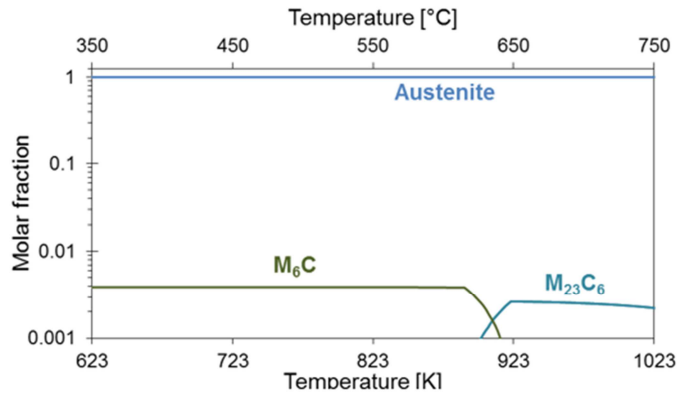
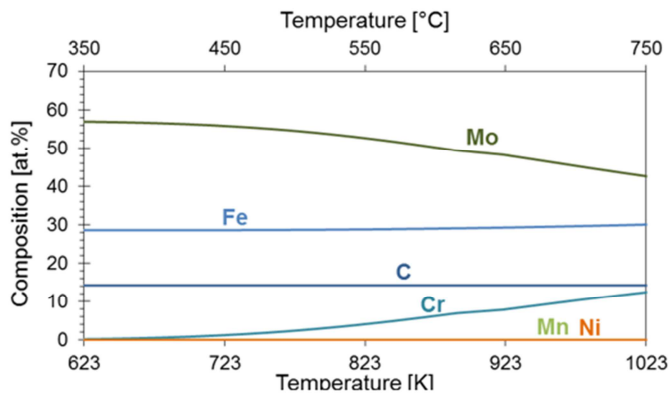
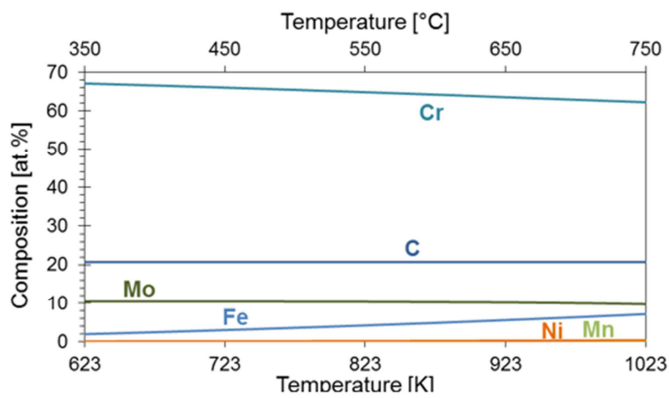
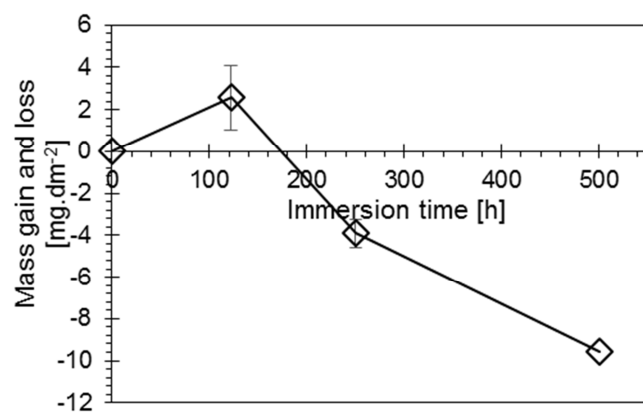
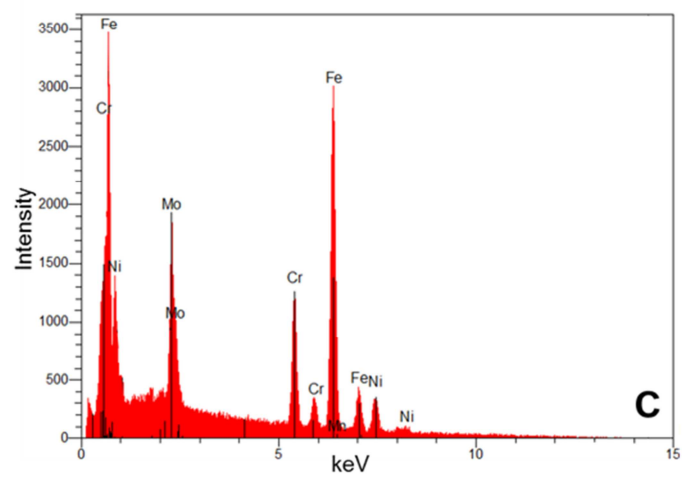
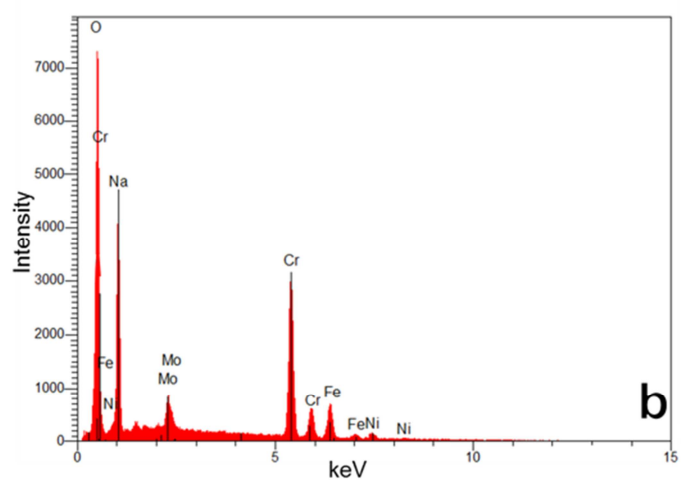
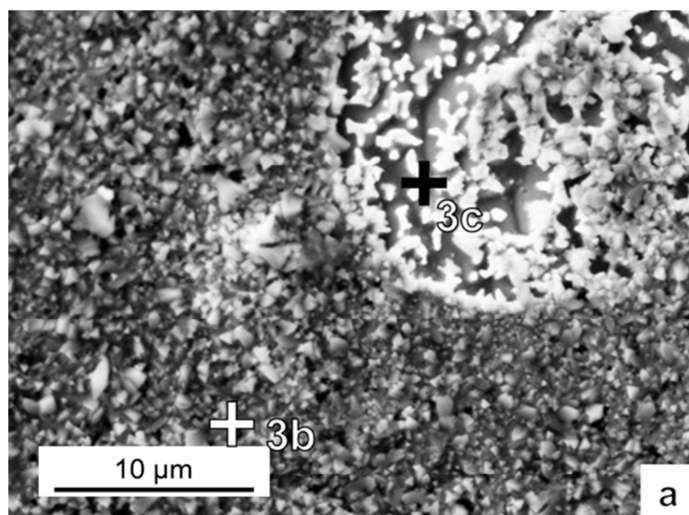


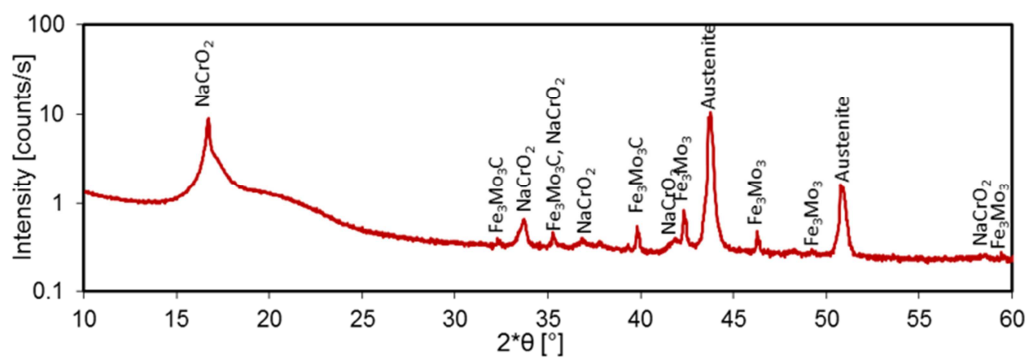
Fig. 11a

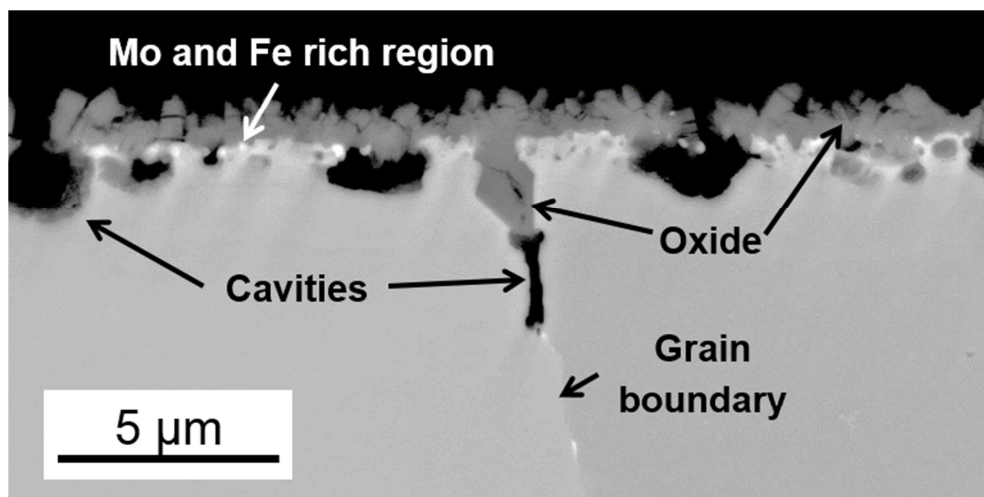
Fig. 11b - M_6C Fig. 11c - $M_{23}C_6$

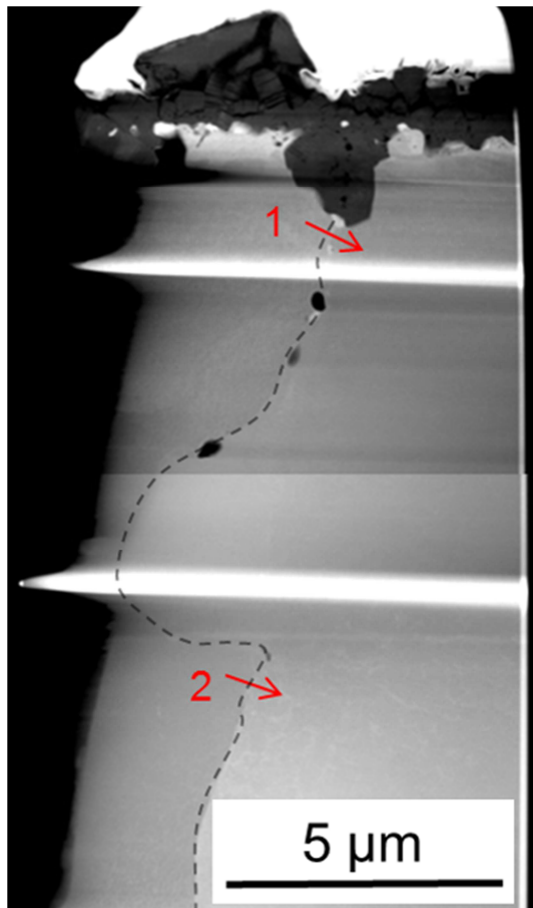


ACCEPTED MANUSCRIPT

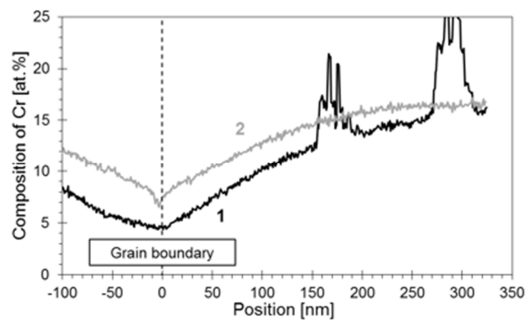




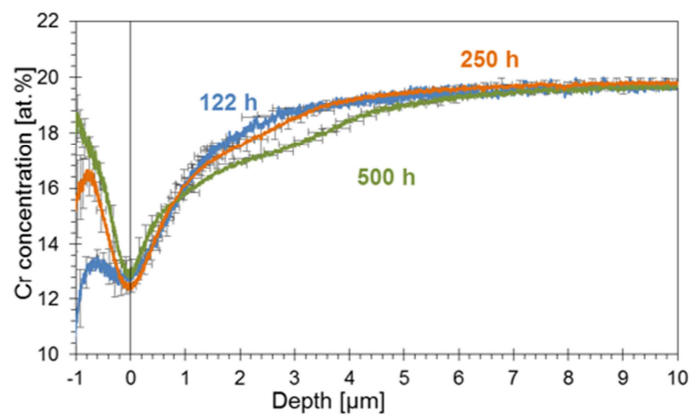




ACCEPTED MANUSCRIPT



ACCEPTED MANUSCRIPT



- Austenitic steel is immersed in liquid sodium containing oxygen at 650°C until 500 h
- NaCrO_2 is formed. O and Na come from liquid metal, Cr from steel
- Mo and Fe rich M_6C carbides are formed. Mo and Fe come from steel, C from liquid metal
- Cavities are also observed. They are due to oxidation, carburization and dissolution
- Cr depletion is observed nearby the surface and in the vicinity of grain boundaries